Steady-state CO oxidation on Pd(111): first-principles kinetic Monte Carlo simulations and microkinetic analysis

Simone Piccinin[1,*], Michail Stamatakis[2,*]

[1] CNR-IOM DEMOCRITOS c/o SISSA, Via Bonomea 265, 34136 Trieste, Italy, Tel.: +39-040-3787317

[2] Department of Chemical Engineering, University College London, Torrington Place London WC1E 7JE, United Kingdom, Tel.: +44-203-1081128

[*] Corresponding authors' e-mails: piccinin@iom.cnr.it, m.stamatakis@ucl.ac.uk

Abstract Using a kinetic Monte Carlo (KMC) approach with parameters derived from first-principles calculations, we modeled the steady-state of CO oxidation on Pd(111), a prototypical catalytic system with various practical applications, including the treatment of automotive gas exhausts. Focusing on the metallic phase of the catalyst, we studied how the rate of CO oxidation depends on temperature and pressure, at fixed gas phase composition. Comparing the results of our simulations with experimental data, we found that all the qualitative features of this catalytic system are correctly reproduced by our model. We show that, when raising the temperature, the system transitions from a CO-poisoned regime with high apparent activation energy to a regime where the rate is almost independent of the temperature. The almost zero apparent activation energy at high temperature stems from approximately equal and opposite values of the O_2 adsorption energy and dissociation barrier, as revealed by a simple microkinetic analysis. In the CO-poisoned regime, the precursor-mediated dissociative adsorption of oxygen plays a crucial role: we find that small changes (within DFT error) in the parameters controlling this elementary step have large effects on the kinetics of CO oxidation at low temperature.

Keywords Kinetic Monte Carlo; CO oxidation; Pd(111); DFT

PACS 68.43.Bc; 82.65.+r; 82.45.Jn

1 Introduction

CO oxidation on Pd is a key reaction taking place in automotive catalytic converters, as well as a prototypical heterogeneous catalytic reaction. Several studies have therefore been dedicated to understand in detail the mechanism of this reaction on Pd as well as on other transition metals like Pt, Rh and Ru. Since the early studies of Ertl and co-workers in the late 70s [1], the reaction on Pd has been shown to proceed through a Langmuir-Hinshelwood (LH) mechanism, whereby both reactants (CO and O) are adsorbed on the metal surface. Most of the works on single crystal Pd catalysts have focused on the (100) facet, where, depending on the conditions of temperature and pressure, the thermodynamically stable phase of catalyst can change from its metallic form to bulk oxide, and even surface oxides have been detected and found to be stable or metastable [2]. The formation of surface oxides on Pd(100) has been shown by Hendriksen *et al.* [3] to result in a change of mechanism, from LH to Mars-van Krevelen (MvK), where oxygen is provided by the oxide, which is continuously depleted and reformed. This transformation was argued to result in an increase of the catalytic activity, while other groups suggested that the most active phase is the metallic one, at conditions where the CO coverage is low, so as not to inhibit O_2 adsorption and dissociation [4,5]. In a recent theoretical work, Hoffmann *et al.* [6] used kinetic Monte Carlo (KMC) simulations based on density functional theory (DFT) calculations to model CO oxidation on the (100) facet, investigating the mechanism of reduction of the surface oxide to a clean metal, with results in good agreement with experiments.

Compared to the (100) facet, the (111) termination has received less attention. As in the case of the (100) facet, Gabasch *et al.* [7] found the metallic phase on the (111) facet to be the most active, compared to both the surface oxide and bulk oxide. In a recent theoretical work, Duan and Henkelman [8] suggested that while on the clean Pd(111) metal surface the reaction proceeds via a LH mechanism, the formation of a surface oxide might be accompanied by a change of mechanism (Eley-Rideal), where chemisorbed O reacts directly with gas-phase CO. Duan and Henkelman also investigated in detail the thermodynamic stability of various surface structures on the (111) facet, concluding that the conditions relevant to practical applications of CO oxidation (pressures of $\sim$ 1 atm, temperatures in the 300-600 K range) are close to those where the surface oxide and the clean metal surface coexist, i.e. where they have similar surface free energy. This finding is in line with what has been established on the (100) facet [9].

In experiments performed at fixed pressure, where the rate of CO_2 formation is monitored as a function of temperature, several groups found an Arrhenius behavior at low temperature, with an apparent activation energy in the 1.0-1.3 eV range on the (100) facet [5,10] and 1.1 eV on the (111) facet [1] at around ambient pressure. As the temperature increases, though, the rate displays a plateau with almost no temperature dependence [7,10] or even a slightly negative apparent activation energy [5]. The temperature at which the transition between the two regimes takes place is pressure dependent, with higher pressures resulting in higher transition temperatures. The high-E^{act} regime has been characterized as being dominated by CO inhibition of the Pd surface. The low-E^{act} regime, at least at high pressure, has been argued to be dominated by mass transfer limitations, where the rate at which gas-phase reactants are supplied to the catalytic surface limits the overall rate of CO oxidation [5].

In this work, we employ kinetic Monte Carlo simulations to model CO oxidation on metallic Pd(111). All the parameters of our simulations are derived from first principles, through DFT calculations. We model O_2 adsorption and dissociation via a molecular precursor mechanism, consistently with experiment. We simulate the system at low pressure, under conditions where the metallic phase is the thermodynamically stable one, and we therefore do not address the role of surface oxides. We focus on the steady state of this catalytic reaction, monitoring the rate dependence as a function of temperature and pressure. Our results are in qualitative agreement with the experimental measurements, and in particular we clearly identify the two regimes (low-E^{act} and high-E^{act}) discussed in the experimental literature [5,10], characterized by vastly different apparent activation energy. We find large quantitative discrepancies in the apparent activation energy in the high-E^{act} regime, and we identify the adsorption and dissociation of oxygen to be crucial in the description of the CO-inhibited region. In particular, the kinetics of oxygen adsorption can be changed from linear to quadratic in the number of vacant sites upon small changes in the adsorption energy of the molecular oxygen precursor and in the activation energy for its dissociation. With the use of simple microkinetic models previously proposed in the literature, we analyze the effects of these changes on the overall kinetics of CO oxidation.

2 Methods

2.1 Kinetic Monte Carlo

In this work we use the Graph-Theoretical kinetic Monte Carlo (GT-KMC) framework as implemented in the software package Zacros [11]. This approach has been illustrated before in our previous works [12-15] and here we briefly summarize the main features.

The energy of the lattice for a given configuration is computed using the cluster expansion approach. The Hamiltonian H of the system is given by:

$$H(\sigma)=\sum_{k=1}^{N_C}\frac{ECI_k}{GM_k}\cdot NCE_k(\sigma) \tag{1}$$

where σ is a vector describing the microscopic configuration of the system (i.e. which sites are occupied by which adsorbates); N_C is the number of figures/clusters specified in the energetic model; ECI_k is the effective cluster interaction of figure k, namely the contribution of one such figure to the total energy; GM_k is the graph-multiplicity of that figure, and NCE_k is the number of occurrences of figure k in the current lattice configuration. GM_k is equal to the number of permutations of lattice site indexes that will result in the detection of the same pattern, i.e. the number of times a distinct pattern is overcounted by the detection algorithm [13]. The ECI_k terms are fitted against DFT calculations, as discussed below.

For each of the possible lattice processes, the rate constant is calculated from an Arrhenius expression of the form:

$$k_{fwd}=\frac{k_B\cdot T}{h}\cdot\frac{Q^{\ddagger}}{Q_R}\cdot\exp\left(-\frac{E_{fwd}^{\ddagger}(\sigma)}{k_B\cdot T}\right), \tag{2}$$

where "*fwd*" denotes the forward step in a reversible event, or just an irreversible event; k_{fwd} is the rate constant thereof; k_B and h are Boltzmann's and Planck's constants, respectively; T is the temperature; $Q^{\ddagger}$ and Q_R are the quasi-partition functions of the transition state and the reactants, respectively. These quasi-partition functions include the translational, rotational and vibrational degrees of freedom (where applicable) [12,16,17]. Finally, $E_{fwd}^{\ddagger}(\sigma)$ is the activation energy at that specific configuration denoted by σ. For a reversible event, the rate of the reverse reaction is:

$$k_{rev}=\frac{k_B\cdot T}{h}\cdot\frac{Q^{\ddagger}}{Q_P}\cdot\exp\left(-\frac{E_{rev}^{\ddagger}(\sigma)}{k_B\cdot T}\right), \tag{3}$$

where Q_P is the quasi-partition function of the products.

The reaction energy ΔE_{rxn} depends on the Hamiltonian of the system before and after the reaction, according to

$$\Delta E_{rxn}(\sigma)=H(\sigma')-H(\sigma)+\Delta E_{gas}, \tag{4}$$

Where σ and σ' are the initial and final lattice configurations respectively. Note that $\sigma' = \sigma + \delta\sigma_{rxn}$, implying that the spectator species configuration does not change. The only change is between reactant and products of that particular reaction. ΔE_{gas} the difference in the gas species energies between final and initial configurations. To ensure microscopic reversibility, the activation energies of the forward and reverse elementary steps must satisfy the following relation:

$$\Delta E_{rxn}(\sigma)=E_{fwd}^{\ddagger}(\sigma)-E_{rev}^{\ddagger}(\sigma'). \tag{5}$$

The activation energies are given by:

$$E_{fwd}^{\ddagger}(\sigma) = \max\left(0, \Delta E_{rxn}(\sigma), E_{fwd,0}^{\ddagger} + \omega \cdot \left(\Delta E_{rxn}(\sigma) - \Delta E_{rxn,0}\right)\right), \tag{6}$$

$$E_{rev}^{\ddagger}(\sigma) = \max\left(-\Delta E_{rxn}(\sigma), 0, E_{rev,0}^{\ddagger} - (1-\omega) \cdot \left(\Delta E_{rxn}(\sigma) - \Delta E_{rxn,0}\right)\right). \tag{7}$$

where $E_{fwd,0}^{\ddagger}$ and $E_{rev,0}^{\ddagger}$ are the activation energies of the forward and reverse step at the zero coverage limit (i.e. when the surface is occupied only by the reacting species), ω is a parameter termed the "proximity factor" [18], which incorporates the linear dependence of the activation energies on the reaction energies, and $\Delta E_{rxn,0}$ is the reaction energy at the zero coverage limit, satisfying:

$$E_{rev,0}^{\ddagger} = E_{fwd,0}^{\ddagger} - \Delta E_{rxn,0}. \tag{8}$$

The linear dependence of the activation energies on the reaction energy $\Delta E_{rxn}(\sigma)$ is due to the Brønsted-Evans-Polanyi (BEP) relationship [19-21].

2.2 DFT calculations

To parameterize the aforementioned energetic and kinetic models, we carried out first-principles calculations using density functional theory (DFT). The DFT calculations presented in this work employ the Perdew-Burke-Ernzerhof (PBE) generalized gradient approximation (GGA) [22] for the exchange and correlation functional. We use a plane wave ultrasoft-pseudopotentials [23] approach as implemented in the Quantum ESPRESSO package [24]. Kinetic energy cutoffs used to represent the electron wave function and density are 27 Ry (367.3 eV) and 200 Ry (2721.1 eV), respectively. We adopt a slab geometry, with four metal layers where the bottom two layers are held fixed in bulk positions. A vacuum of around 12 Å ensures negligible coupling between periodic replicas of the slab. The Brillouin-zone integration is performed using equispaced points equivalent to a (12×12×1) regular mesh in the (1×1) surface unit cell, and the Fermi surface is broadened using a smearing parameter of 0.03 Ry (0.41 eV). All the structures are fully relaxed until the forces on all atoms are below 5×10^{-4} a.u. (0.026 eV/Å). The minimum energy paths and the transition states are calculated using the climbing-image nudged elastic band (CI-NEB) approach [25], with a convergence threshold on forces perpendicular to the path of 0.05 eV/Å. The normal mode analysis is performed at the initial and transition states using the finite displacements method, with a displacement of 0.01 Å.

3 Results and discussion

3.1 Construction of the cluster expansion

In our model for CO oxidation on Pd(111) we consider three kinds of adsorbates, CO, O_2 and O, which can occupy two types of sites, the FCC and HCP hollow sites. In the cluster expansion, in addition to on-site adsorption energies, we consider 2-body and 3-body lateral interactions among O-O, O-CO and CO-CO adsorbates, while the interactions between O_2 and all species are modeled using only 2-body terms. The 2-body terms include 1st, 2nd and 3rd nearest-neighbor interactions, while 3-body terms include linear, triangular and bent figures [26,14]. The total number of figures included in our CE is 88, fitted against 105 DFT calculations, with varying number of O and CO adsorbates in (2×2), (3×3) and (4×4) cells. The root mean square error between the DFT and CE estimate of the adsorption energy per adsorbate is 12.3 meV, in line with the 9.6 meV obtained in our previous work were O_2 was not considered as an adsorbate [14]. Further validation of the CE is provided in the Supplementary Information (Section 5).

3.2 NEB calculations

The calculations to compute the activation energy for CO oxidation, O and CO diffusion, have been discussed in our earlier publication [14]. Here we focus on the elementary steps involving O_2 diffusion and dissociation. Experimentally, it has been established that on the (111) facet of Pt-group metals [27-29], and

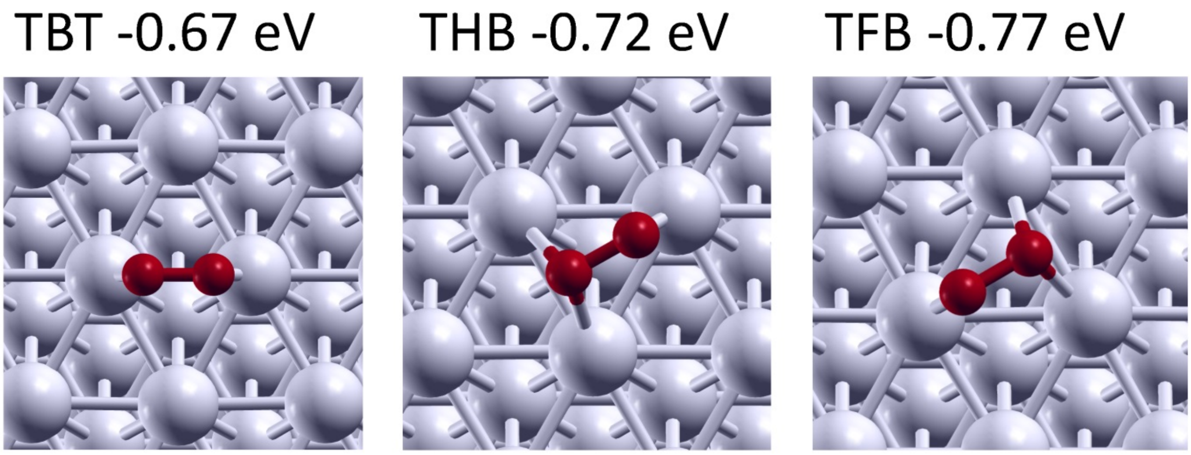

Fig. 1 Adsorption configurations for O_2 adsorption on Pd(111). Top-Bridge-Top (TBT), Top-HCP-Bridge (THB) and Top-FCC-Bridge (TFB) configurations are shown.

in particular on Pd(111) [30,31], oxygen dissociation takes place via a precursor mechanism. In our simulation the dissociation of O_2 is therefore a two step process, involving first the adsorption of O_2^*, followed by the dissociation into two O^* adsorbates. The same model has been considered in a variety of theoretical simulations, both on metal and oxide surfaces [32,33,8,34,35,21].

In agreement with what has been established in previous theoretical works for O_2 adsorption on the (111) surface of Pt-group metals [36,37,33], we find that O_2 can adsorb on Pd(111) in several configurations with similar adsorption energy. In particular we identified the Top-Bridge-Top (TBT), Top-HCP-Bridge (THB) and Top-FCC-Bridge (TFB) configurations with an adsorption energy of −0.67 eV, −0.72 eV and −0.77 eV, respectively (see Fig. 1). Here the adsorption energy is evaluated in a 3×3 supercell and is defined as:

$$E_{ads} = E^{\mathrm{O_2/Pd(111)}} - E^{\mathrm{Pd(111)}} - E^{\mathrm{O_{2(g)}}}, \tag{9}$$

where $E^{\mathrm{O_2/Pd(111)}}$ is the total energy of the adsorption system, $E^{\mathrm{Pd(111)}}$ is the total energy of the clean slab and $E^{\mathrm{O_{2(g)}}}$ is the total energy of an isolated O_2 molecule in gas phase. The differences between our computed adsorption energies and the ones reported by previous works [37] are of the order of 0.2 eV, and are likely due to the different unit cells adopted.

Since the TBT configuration is the least favorable, we will not consider it as a possible adsorption configuration in our model. The dissociation paths we considered are (*i*) from the O_2^* in the TFB configuration two O^* adsorbates on HCP sites and (*ii*) from the O_2^* in the THB configuration two O^* adsorbates on FCC sites. The activation energy, evaluated in a (3×3) unit cell, for the first path is 0.79 eV, while for the second path it is 0.65 eV. The reaction energy for the first reaction is −0.95 eV and for the second reaction is −1.31 eV. In agreement with the BEP principle, we can see that lower barriers correspond to more exothermic reactions.

To evaluate the proximity factor ω we focused on the $O^*_{2,TFB} \rightarrow 2O^*_{HCP}$ reaction and considered the coadsorption of either one or two O^* adsorbates, in different positions. We computed 6 different reaction paths and in Fig. 2 we show the linear fit of the activation energy as a function of the reaction energy, yielding a proximity factor of 0.43. In the following, we assume the same value for proximity factor also for the $O^*_{2,THB} \rightarrow 2O^*_{FCC}$ reaction.

We then considered the diffusion of O_2^* on the surface: $O^*_{2,TFB} \leftrightarrow O^*_{2,THB}$, obtaining an activation energy of 0.10 eV for the forward reaction. In this case, the proximity factor was set to 0.5, as in the case of diffusion of O^* and CO^*.

We note that the theoretical modelling of O_2 adsorption and dissociation on Pt-group metal surfaces has being thoroughly investigated in the recent past [38]. Pt(111), in particular, is the surface that has received most attention, and where a detailed comparison between theory and experiments has been made [39]. Tight-

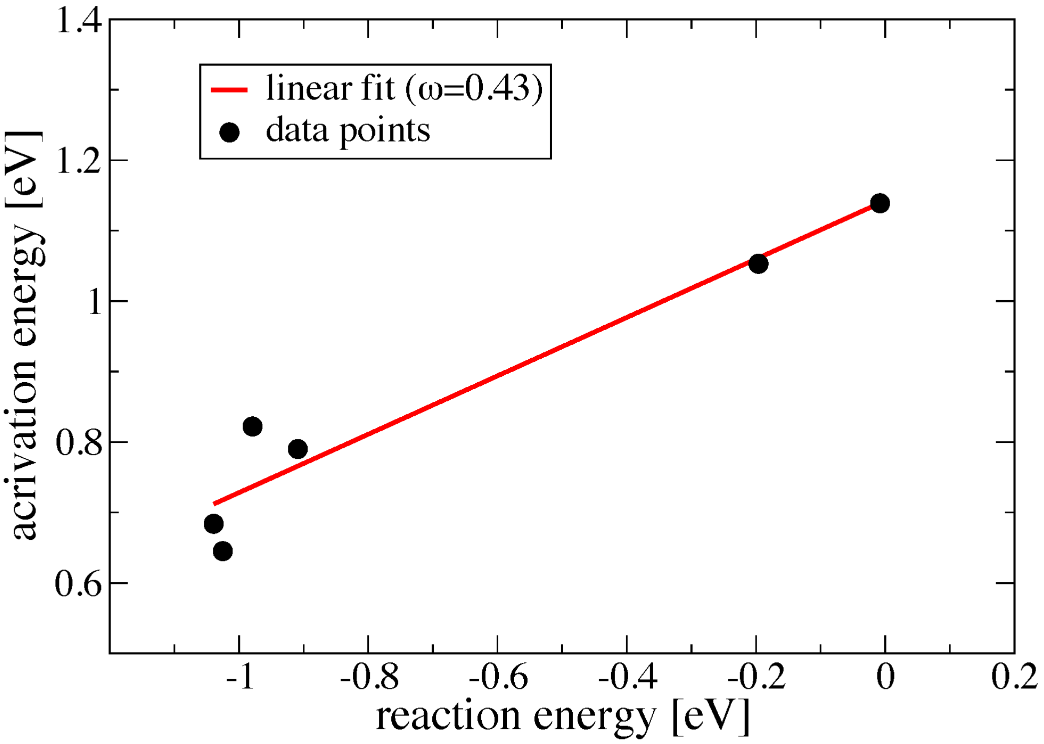

Fig. 2 Linear fit of the activation energy for O_2^* dissociation on Pd(111) as a function of the reaction energy. We consider the reaction $O^*_{2,TFB} \rightarrow 2O^*_{HCP}$ and the reaction energy is defined as the energy difference between final and initial state. The structures differ in the number and position of O^* adsorbates surrounding the dissociating O_2^* molecule.

binding molecular dynamics based on a DFT parameterization, in particular, led to satisfactory agreement between the simulated and the experimental sticking coefficient of O_2. Nonetheless, it is worth recalling that the description of this system is strongly dependent on the exchange and correlation functional employed: for example, going from the PBE to RPBE functional the adsorption energy of O_2 changes from −0.6 eV to −0.1 eV [38].

3.3 KMC simulations

The list of elementary events included in our model is presented in Table 1. Besides adsorption and desorption of CO and O_2, we consider the dissociation of O_2^*, the diffusion of O^*, CO^* and O_2^* and the oxidation of CO^* to CO_2. The O_2^* adsorbate is considered as a monodentate species, with $O^*_{2,TFB}$ treated as an adsorbate on the FCC site and $O^*_{2,THB}$ as an adsorbate on the HCP site.

The CO adsorption energy obtained using DFT-PBE severely overestimates the experimental value, while calculations based on the random-phase approximation (RPA) are in better agreement with experiments [40]. We therefore employed the RPA value (1.5 eV [40]) rather than the PBE value (1.9 eV), and tested the effect that a variation of the CO adsorption energy has on the kinetics of CO oxidation (see Section 3.3.2).

For computational efficiency, we slow down quasi-equilibrated elementary steps that are considerably faster than the fastest non-quasi-equilibrated elementary step. We do so altering the prefactor for such fast events (like diffusions and adsorptions/desorptions), namely scaling the prefactor by a “stiffness coefficient”, ensuring that they are still quasi-equilibrated and at least 2 orders of magnitude faster than the slowest elementary events. As an example, at 400 K, $p_{tot} = 10^{-8}$ bar ($CO:O_2 = 2:1$ molar fraction) we used a stiffness coefficient of 10^4 for CO and O_2 adsorption, 10^6 for O^* and O^* diffusion, 10^{12} for CO^* diffusion. We show in the Supplementary Information that the effect of the stiffness coefficients on the rate of CO oxidation is negligibly small.

Step	A^{fwd} (s^{-1})	A^{fwd}/A^{rev}	E_0^{act} (eV)	ω
$CO_{(g)} + *_{FCC} \leftrightarrow CO^*_{FCC}$	5.69×10^{-5}	0.92×10^{-17}	0	0
$CO_{(g)} + *_{HCP} \leftrightarrow CO^*_{HCP}$	5.69×10^{-5}	1.88×10^{-17}	0	0
$CO^*_{FCC} + *_{HCP} \leftrightarrow *_{FCC} + CO^*_{HCP}$	5.37×10^{-1}	1.39	0.26	0.5
$O_{2(g)} + *_{FCC} \leftrightarrow O^*_{2,FCC}$	2.66×10^{-5}	1.88×10^{-17}	0	0
$O_{2(g)} + *_{HCP} \leftrightarrow O^*_{2,HCP}$	2.66×10^{-5}	1.75×10^{-17}	0	0
$O^*_{2,FCC} + *_{HCP} \leftrightarrow *_{FCC} + O^*_{2,HCP}$	2.03×10^{6}	0.93	0.10	0.50
$O^*_{2,FCC} + 2*_{HCP} \leftrightarrow 2O^*_{HCP} + *_{FCC}$	1.42×10^{13}	0.39	0.79	0.43
$O^*_{2,HCP} + 2*_{FCC} \leftrightarrow 2O^*_{FCC} + *_{HCP}$	1.53×10^{13}	0.23	0.65	0.43
$O^*_{FCC} + *_{HCP} \leftrightarrow *_{FCC} + O^*_{HCP}$	7.87×10^{6}	1.36	0.53	0.50
$CO^*_{FCC} + O^*_{FCC} \leftrightarrow CO_{2(g)}$	3.13×10^{13}	-	1.13	0.33
$CO^*_{HCP} + O^*_{HCP} \leftrightarrow CO_{2(g)}$	1.14×10^{13}	-	1.08	0.33

Table 1 List of the elementary steps included in the KMC model, including the prefactor in the forward direction (A^{fwd}) at 400 K and $p_{tot} = 10^{-8}$ bar; the ratio of the prefactors in the forward and backward directions; the activation energy in the zero-coverage limit (E_0^{act}); and the proximity factor (ω).

3.3.1 Effects of temperature and pressure

In Fig. 3 we show the rate of CO oxidation (turnover frequency, TOF) as a function of temperature for three values of total pressure: 10^{-10}, 10^{-8} and 10^{-6} bar, while keeping the CO:O_2 mole ratio fixed at 2:1. Plotting the log of the TOF against inverse temperature we obtain at low temperature an Arrhenius behavior, with an approximately linear drop of the TOF yielding an apparent activation energy of 1.66 ± 0.06 eV at 10^{-10} bar, 1.69 ± 0.05 eV at 10^{-8} bar and 1.78 ± 0.04 eV at 10^{-6} bar. At higher temperature, on the other hand, the TOF saturates, resulting in very small apparent activation energies (0.12 ± 0.01 eV at 10^{-10} bar). The temperature at which such saturation occurs clearly moves towards higher temperatures as the pressure increases.

To rationalize these results we first of all monitored the rates of all the elementary events considered in our simulations for two values of temperature, 400 K and 600 K, representative of the high- and low-E^{act} regimes, respectively, and two values of pressure, 10^{-6} and 10^{-10} bar (see Supplementary Information, Section 2.1). This analysis shows that at all conditions the CO oxidation reaction and the O^* dissociation have a similar rate and in both cases the forward reaction dominates, making them essentially irreversible. Moreover, all the other elementary steps (i.e. CO^*, O^* and O_2^* diffusion, CO and O_2 adsorption) are quasi-equilibrated.

We then computed the degree of rate control [41] X_{RC} defined as

$$X_{\mathrm{RC,n}} = \frac{\partial \log(\mathrm{TOF})}{\partial\left(\frac{-E_n^0}{RT}\right)}, \qquad (10)$$

through finite differences at 390 K, taking E_n^0 to be: *(i)* the adsorption energy of O_2^* on HCP sites; *(ii)* the activation energy for dissociation of O_2^* on HCP sites; *(iii)* the adsorption energy of CO^* on FCC sites; *(iv)* activation energy for CO oxidation of adsorbates on FCC sites. We varied E_n^0 by ± 0.05 eV and computed the corresponding TOF. For these four cases we obtained values for X_{RC} of 0.75, 0.70, 0.90 and 0.02. We can therefore conclude that in the high-E^{act} regime the surface reaction of CO oxidation is not rate limiting, while O_2^* dissociation is. Moreover, the adsorption energy of the molecular oxygen precursor and CO^* have large X_{RC} values, showing that the stability of these intermediates is a key factor in the kinetics of the overall process.

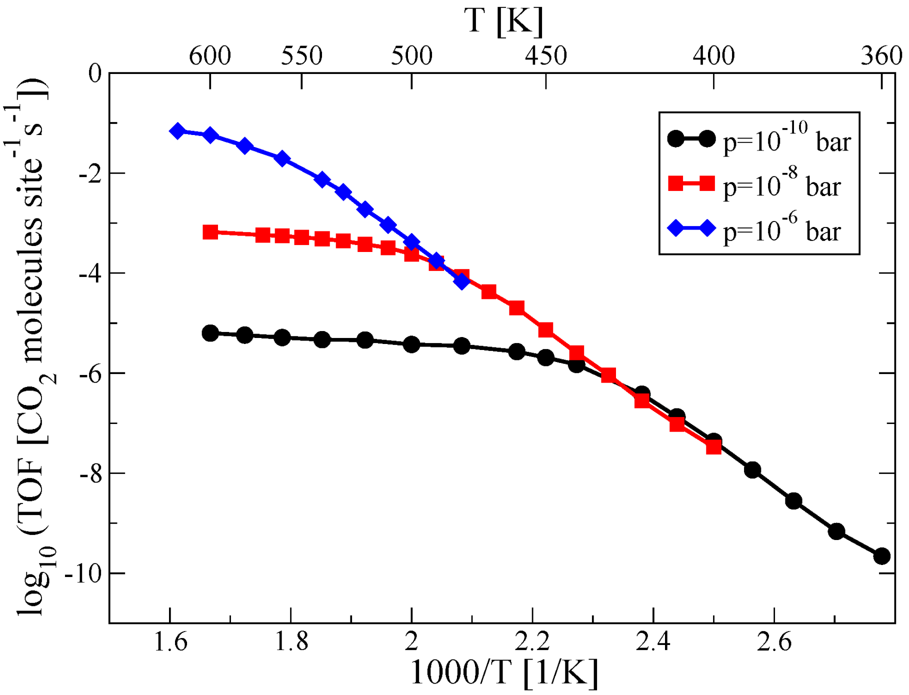

Fig. 3 Arrhenius plot of the temperature dependence of the rate of CO oxidation, computed for three values of pressure while keeping the CO:O_2 mole ratio fixed at 2:1.

Further insights are offered by monitoring the coverages of the adsorbates at various conditions of temperature and pressure. In Fig. 4 we show the coverage of O^* and CO^* (considering the sum of adsorbates on both FCC and HCP sites) as a function of temperature for three values of pressure, 10^{-6}, 10^{-8} and 10^{-10} bar. The coverage of O_2^* is not shown, since it is negligibly small in the range of temperatures and pressures examined here. The high-E^{act} regime is therefore characterized by a high CO^* coverage (CO^* inhibition, in agreement with experiment), while at high temperature the coverages of both adsorbates are small. As the pressure increases, Fig. 4 shows that the temperature at which the CO^* coverage drops to zero moves to higher values, which explains why the transition from the low-E^{act} to the high-E^{act} regime happens at higher temperatures. All the qualitative features of our simulations reproduce well the experiments performed by Goodman and co-workers [5], who monitored the TOF of CO oxidation on Pd(100) in the CO pressure range 10^{-8} - 8 Torr, using a 2:1 CO:O_2 mole ratio as in our simulations. Unfortunately, an experimental dataset is not available for the (111) facet, but comparison of the TOF vs. temperature for the (111) and (100) facets at a fixed CO pressure of 10^{-6} Torr shows a remarkably similar behavior [5], in agreement with the fact that CO oxidation on Pt-group catalysts is known to be structure insensitive [42].

Comparing the absolute values for the TOF we have obtained in our simulations with those obtained

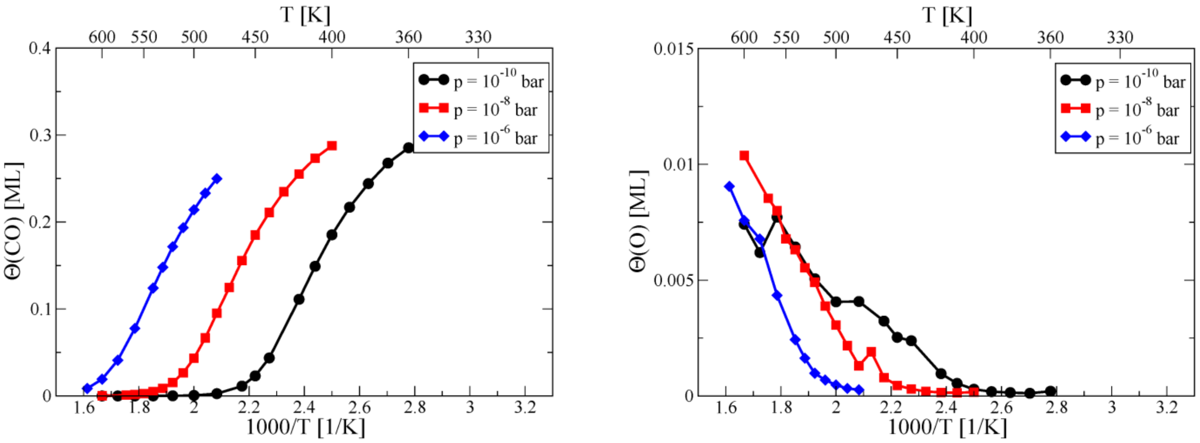

Fig. 4 Steady state coverages of CO^* (left) and O^* (right) as a function of temperature reported for three values of pressure, with Eb(CO) = 1.5 eV. Discontinuities on the coverage are due to statistical errors.

experimentally on the Pd(100) surface [5,10], our computed rates are about 3 orders of magnitude lower than the experimental values. This discrepancy could be due to errors in the activation energies and adsorption energies used in our simulations. As an example, an error of 0.2 eV in the activation energy of a rate determining step, an error compatible with the accuracy of DFT-GGA calculations, would lead to changes in the rate of that process at 400 K of the same order as the discrepancy mentioned above ($e^{-0.2/k_BT} \approx 3\times10^{-3}$ at T = 400 K).

More disconcerting, on the other hand, is the fairly large discrepancy between the apparent activation energy in the CO*-inhibited region measured experimentally, 0.64 eV at a total pressure of 10^{-10} bar [5], and the one extracted from our simulations, 1.66 - 1.78 eV. In the following, we explore two possible sources of this discrepancy, namely an inaccurate value of the adsorption energy of CO* and an unreliable model for the dissociation of O_2^*.

3.3.2 Effects of CO adsorption energy

In this Section we investigate the effect of the adsorption energy of CO* on the catalytic properties of the system. On the basis of the large degree of rate control X_{RC} discussed earlier, we expect the stability of the CO* adsorbate to be crucial in the kinetics of the overall process. Experiments as well as DFT-RPA calculations [40] suggest a value of around –1.5 eV for the CO adsorption energy on Pd(111) hollow sites in the low coverage limit. We performed a series of simulations where we varied this quantity while leaving all the other parameters of the calculations unchanged. We show in Fig. 5 the effect of making the CO* adsorption on Pd(111) weaker than the experimental value, by comparing the results of the simulations described in the previous section (E_b(CO) = –1.5 eV) with those where E_b(CO) was set to –1.4 eV and –1.3 eV (i.e. where we reduced the strength of the CO adsorption on both FCC and HCP sites by 0.1 and 0.2 eV). At high temperature, weakening the CO* interaction with the surface has the effect of reducing the TOF, as a result of the lower CO* coverage. At low temperature, in the CO-inhibited region, the apparent activation energy decreases substantially when CO* is bound less strongly. We obtain values for the apparent activation energy of 1.66 eV, 1.37 eV and 1.02 eV with values for E_b(CO) of –1.5 eV, –1.4 eV and –1.3 eV, respectively. In Fig. 6 we present a comparison of the steady state coverages for CO* and O* with values of E_b(CO) of –1.5, –1.4 and –1.3 eV. Not surprisingly, at fixed temperature, the CO* coverage decreases as the interaction of CO* is weakened, while the opposite happens for the coverage of O*.

This analysis shows that increasing E_b(CO) has a large effect on the kinetics of this system in the CO-inhibited region. Allowing for deviations of E_b(CO) 0.1-0.2 eV, however, is not enough to reconcile our KMC model with the experimental measurements of the apparent activation energy. To understand the

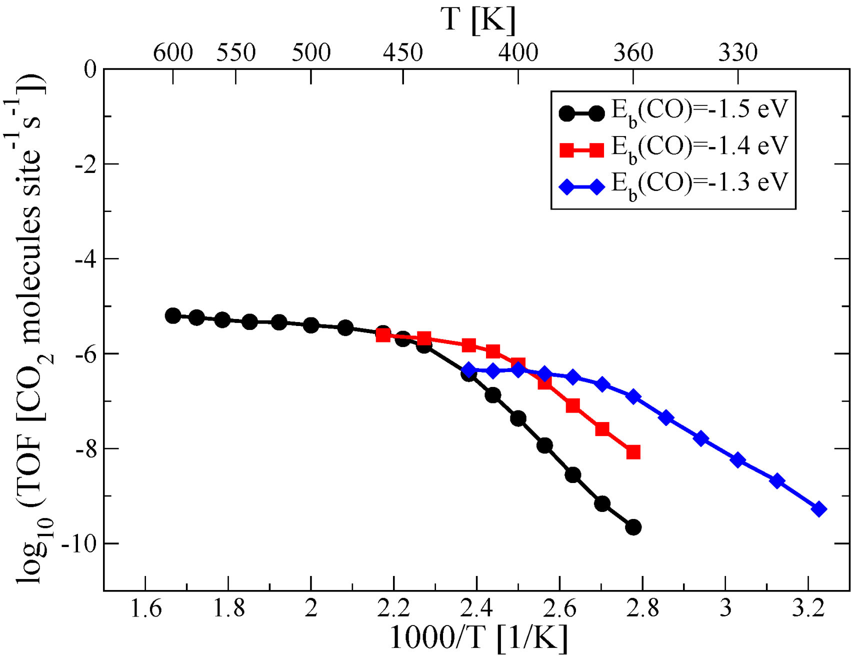

Fig. 5 Arrhenius plot of the temperature dependence of the rate of CO oxidation, computed for three values of CO* adsorption energy. The total pressure is set to 10^{-10} bar and the CO:O_2 mole ratio is 2:1.

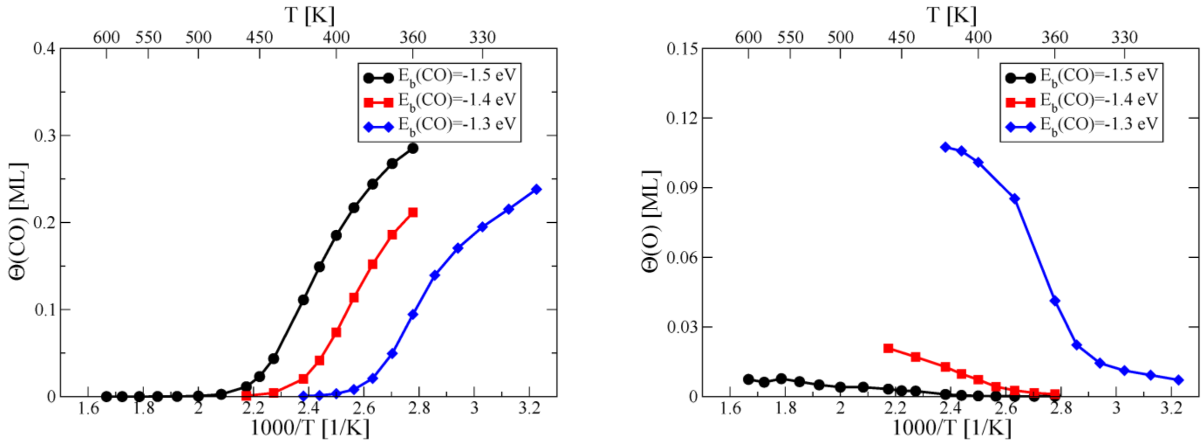

Fig. 6 Steady state coverages of CO^* (left) and O^* (right) as a function of temperature reported for three values of E_b(CO). The total pressure is set to 10^{-10} bar and the CO:O_2 mole ratio is 2:1.

relation between the adsorption energy of CO^* and the apparent activation energy of CO oxidation, Xu and Goodman [43] developed a microkinetic model that consists of the following four elementary steps:

$$CO_g \rightarrow CO^* \qquad k_1 \tag{11}$$

$$CO^* \rightarrow CO_g \qquad k_2 \tag{12}$$

$$O_{2,g} \rightarrow 2O^* \qquad k_3 \tag{13}$$

$$O^* + CO^* \rightarrow CO_{2,g} + 2* \qquad k_4 \tag{14}$$

where k_i is the rate constant of each elementary step. Assuming the rate of O_2 adsorption to be linear in the number of empty sites, i.e.

$$\frac{d\theta_{O^*}}{dt} = 2k_3 p_{O_2} \theta_*, \tag{15}$$

Xu and Goodman [43] found that the apparent activation energy of the CO oxidation reaction in the CO-inhibited region is equal to the adsorption energy of CO. Other microkinetic models proposed in the literature for CO oxidation on Pt-group catalysis, on the other hand, lead to different apparent activation energies. The model adopted by Falsig *et al.* [32] and by Duan and Henkelman [8] consists of the following four elementary steps:

$$CO_g \leftrightarrow CO^* \tag{16}$$

$$O_{2,g} \leftrightarrow O_2^* \tag{17}$$

$$O_2^* \rightarrow 2O^* \tag{18}$$

$$O^* + CO^* \rightarrow CO_{2,g} + 2* \tag{19}$$

Assuming the coverage of adsorbed atomic oxygen θ_{O^*} to be negligibly small (a good approximation in the CO-inhibited region), the CO and O_2 adsorption/desorption reactions to be quasi-equilibrated and the O_2^* dissociation to be non-reversible (good approximations, as shown in the Supplementary Information Fig. 3), the steady state rate of CO oxidation has the following expression:

$$r_{CO}^{oxid} = 2k_{O_2}^{diss} \theta_{O_2^*} \theta_* \tag{20}$$

$$= 2A^{fwd} e^{-E^{act}_{O_2,diss}/k_B T} \frac{K_{O_2}^{ads} p_{O_2}}{\left[1 + K_{CO}^{ads} p_{CO} + K_{O_2}^{ads} p_{O_2}\right]^2} \tag{21}$$

where K's are the equilibrium constants and A^{fwd} is the prefactor for the dissociation of O_2^*. If we take the high-temperature and low-temperature limits of this expression, we find:

$$E_{app}^{high-T} = k_B \lim_{T\to\infty} \frac{\mathrm{d}}{\mathrm{d}(1/T)} \log\left(r_{\mathrm{CO}}^{oxid}\right) = -\left(E_b\left(\mathrm{O}_2\right) + E_{\mathrm{O}_{2,\mathrm{diss}}}^{act}\right) \tag{22}$$

$$E_{app}^{low-T} = k_B \lim_{T\to 0} \frac{\mathrm{d}}{\mathrm{d}(1/T)} \log\left(r_{\mathrm{CO}}^{oxid}\right) = -\left(E_b\left(\mathrm{O}_2\right) + E_{\mathrm{O}_{2,\mathrm{diss}}}^{act} - 2E_b\left(\mathrm{CO}\right)\right) \tag{23}$$

From these two expressions it is clear why in Fig. 3 the apparent activation energy at high temperature is nearly zero, since in our KMC model we have $E_{\mathrm{O}_{2,\mathrm{diss}}}^{act}$ = 0.65 eV and $E_b\left(\mathrm{O}_2\right)$ = –0.67 eV in the zero-coverage limit. At low temperature, on the other hand, this microkinetic model gives an apparent activation energy that is approximately equal to $2E_b(\mathrm{CO})$, at variance with the model of Xu and Goodman. The crucial difference in the two microkinetic models giving rise to this difference is how O_2 adsorption and dissociation is treated. As shown in Eq. 15, Xu and Goodman assume that the adsorption rate of oxygen $\mathrm{d}\theta_{\mathrm{O}^*}/\mathrm{d}t$ is linear in the vacant sites θ^*, while the model of Falsig *et al.* leads to a quadratic dependence. It is therefore crucial to examine which model is more appropriate and what kind of kinetics for O_2 adsorption and dissociation we obtain in our KMC simulations.

3.3.3 O_2 adsorption and dissociation: Effects of adsorption energy and dissociation barrier

A distinctive feature of O_2 adsorption and dissociation on the (111) facet of Pt-group metals is the fact that this process occurs via a precursor [27-31], as discussed in Section 3.2. Xu and Goodman [43] suggested that the presence of a precursor implies that the rate of oxygen adsorption in linear in vacant surface sites. This was indeed shown by Yates *et al.*, [28] who found that the adsorption rate for O_2 on Rh(111) at 335 K is proportional to $1–\Theta$, while the authors expected a $(1–\Theta)^2$ dependence, since two O^* adsorbates need to be accommodated (here Θ here indicates the O^* coverage).

Assuming a $(1–\Theta)^2$ dependence would lead to $\Theta/(1–\Theta)$ being linear in the O_2 exposure, while a $(1–\Theta)$ dependence would lead to $–log(1–\Theta)$ being linear in the O_2 exposure. Following Yates *et al.* [28], in Fig. 7(a) we plot these two quantities against O_2 exposure using the cluster expansion fitted against our DFT data as discussed in Section 3.1 and the activation energies for O_2 dissociation discussed in Section 3.2. The red dashed line in Fig. 7(a) shows the quantity $\Theta/(1–\Theta)$, while the black solid line shows $–log(1–\Theta)$. This simulation shows clearly that the red dashed line is approximately linear, while the solid black line is not,

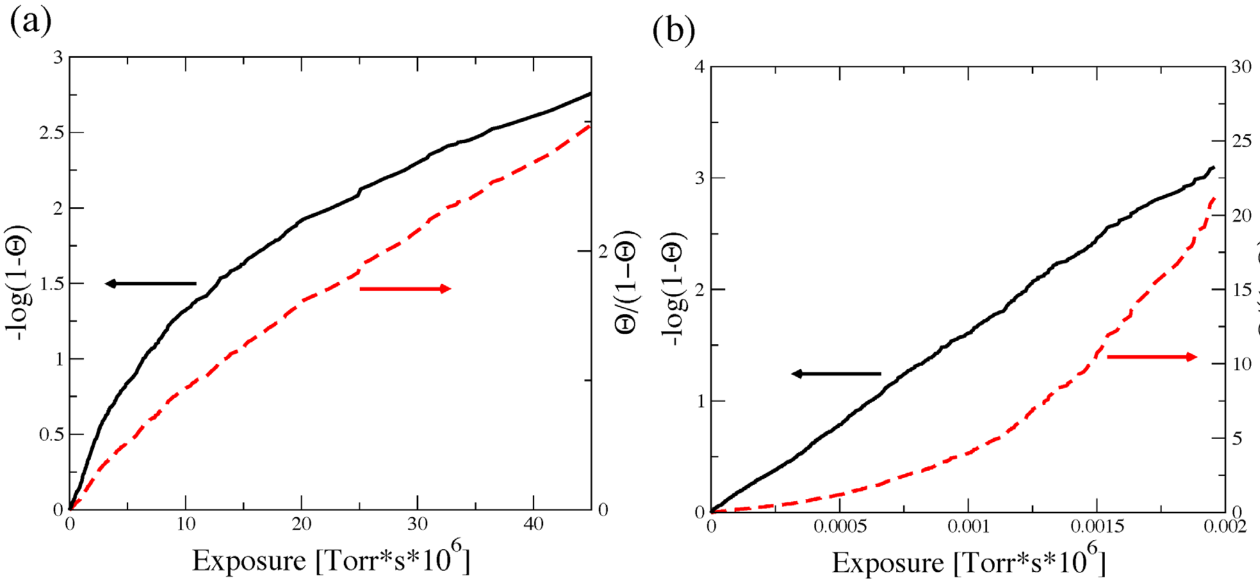

Fig. 7 Plot of the O^* coverage Θ as a function of the O_2 exposure (p_{O_2}[Torr]×time[s]×10^6). The red dashed line is a plot of the quantity $\Theta/(1–\Theta)$ while the black solid line is the quantity $–\log(1–\Theta)$. Panel (a) is obtained from a simulation with the original parameters for O_2 adsorption and dissociation ($E_{\mathrm{O}_{2,\mathrm{diss}}}^{act}(\mathrm{FCC}) = 0.79\,\mathrm{eV}$, $E_{\mathrm{O}_{2,\mathrm{diss}}}^{act}(\mathrm{HCP}) = 0.65\,\mathrm{eV}$, $E_b(\mathrm{O}_2,\mathrm{FCC}) = -0.67\,\mathrm{eV}$, $E_b(\mathrm{O}_2,\mathrm{HCP}) = -0.52\,\mathrm{eV}$), while in panel (b) we employed $E_{\mathrm{O}_{2,\mathrm{diss}}}^{act}(\mathrm{FCC}) = 0.59\,\mathrm{eV}$, $E_{\mathrm{O}_{2,\mathrm{diss}}}^{act}(\mathrm{HCP}) = 0.45\,\mathrm{eV}$, $E_b(\mathrm{O}_2,\mathrm{FCC}) = -0.97\,\mathrm{eV}$, $E_b(\mathrm{O}_2,\mathrm{HCP}) = -0.82\,\mathrm{eV}$.

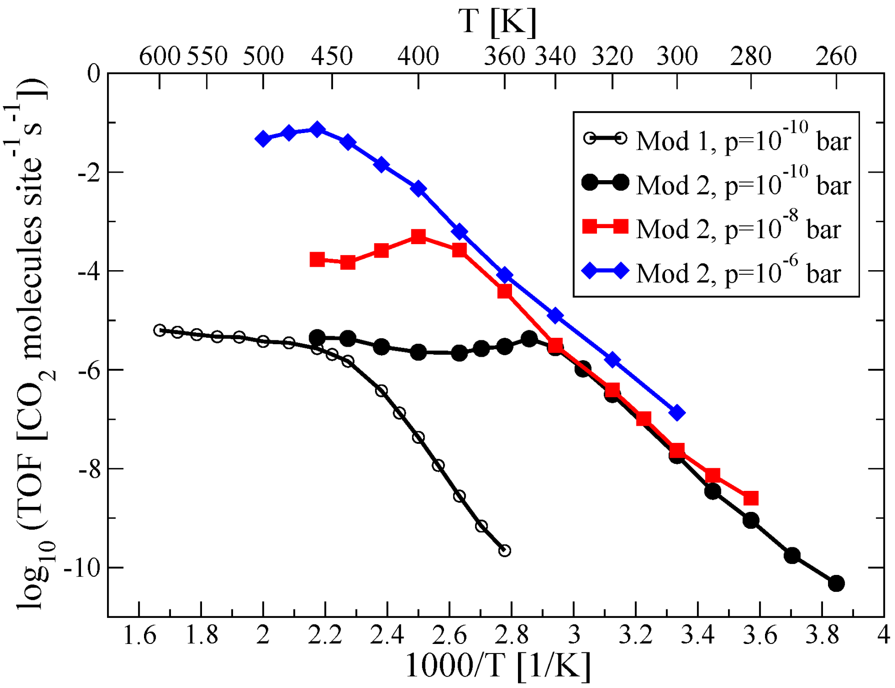

Fig. 8 Comparison of the TOF of CO oxidation obtained with two different sets of parameters for O_2 adsorption and dissociation: Model 1 uses the original cluster expansion derived from DFT calculations described and the activation energy for O_2 dissociation obtained from the NEB calculations (here we show only the results at $p_{tot} = 10^{-10}$ bar; Model 2 uses an adsorption energy for O_2^* lowered (i.e. more strongly bound) by 0.3 eV and an activation energy for O_2 dissociation lowered by 0.2 eV.

implying that with our theoretical model adsorption of O_2 is proportional to $(1-\Theta)^2$, at variance with the experimental findings. As discussed earlier, a quadratic dependence implies that the apparent activation energy in the CO-inhibited region is ~ $2E_b$(CO), and this is the most likely cause for the high apparent activation energy in our KMC simulations.

In an attempt to reproduce the linear O_2 dissociation kinetics, we subsequently varied the on-site adsorption energy of O_2^* and the activation energy of the dissociation of O_2^*. We thus found that fairly small changes in these parameters can lead to different kinetics for the O_2 adsorption, which is consistent with the large degree of rate control X_{RC} of these two parameters. In particular, lowering the activation energy (of both the FCC and HCP paths) by 0.2 eV and increasing the strength of O_2^* adsorption (on both FCC and HCP sites) by 0.3 eV leads to the results shown in Fig. 7(b), which are indicative of adsorption kinetics linear in $(1-\Theta)$, in agreement with experiments. We stress that errors of the orders of 0.2-0.3 eV in adsorption energies and activation energies are compatible with typical error in DFT simulations based on GGA functionals.

The impact that these changes on the on-site adsorption energy of O_2^* and the activation energy of the dissociation of O_2^* have on the kinetics of CO oxidation is displayed in Fig. 7. While qualitatively the overall shape of the TOF vs. 1/T curves are similar when comparing the original simulation in Fig. 3 with the one obtained with the modified values for O_2^* adsorption and dissociation, the effect is an overall shift of these curves towards lower temperatures and a sensible reduction of the activation energy in the CO-inhibited region, from 1.66 ± 0.06 eV to 0.92 ± 0.08 eV, now in better agreement with the experimental estimate of 0.64 eV at a pressure of 10^{-10} bar [5]. On the basis of the microkinetic models described above, we can ascribe this reduction in apparent activation energy to a change in the kinetics of O_2 adsorption and desorption, triggered by the small but relevant changes in the O_2^* adsorption energy and barrier for dissociation.

We stress that we cannot expect quantitative agreement between the predictions of these microkinetic models and the full KMC simulations, as further discussed in the Supplementary Information. The reason is that they only consider one type of adsorbate, and completely neglect interactions among adsorbates as well as the effects of such interactions on the activation energies; these simplifications severely limit the ability of these models to achieve an accurate quantitative description of the kinetics of the system. Yet, as we saw, these microkinetic models were extremely important in rationalizing the behavior of the catalytic system.

4 Conclusions

In this work, we modeled the steady-state of CO oxidation on Pd(111) using a kinetic Monte Carlo approach with parameters derived from first-principles calculations. We studied how the TOF depends on temperature and pressure, keeping the CO:O_2 mole ratio set at 2:1 and focusing on conditions where the catalyst remains in its metallic phase. Comparing the results of our simulations with experimental data, most of which are available only for the (100) facet, we found that all the qualitative features of this catalytic system are faithfully reproduced by our model. In particular, we correctly identified two regimes, at low and high temperature, characterized by vastly different apparent activation energies. The dependence of the TOF on pressure as well as the dependence of the temperature at which the system transitions between the two regimes on pressure are also correctly captured.

In agreement with experiments, we find that the high-E^{act} regime is characterized by CO-inhibition. The low-E^{act} regime, on the other hand, displays a plateau, as a result of the adsorption energy of O_2 and the activation energy for O_2 dissociation being approximately equal in magnitude and opposite in sign. Using our original parameter set, we found large quantitative discrepancies between our simulations and the experimental measurements, both in the absolute values of our TOFs as well as in the apparent activation energy in the low temperature regime. These discrepancies are likely due to errors in the DFT-derived parameters that enter our model. In particular we have shown that the O_2 adsorption and dissociation predicted by our model is quadratic in the vacant sites, while experimental measurements show it is linear. Small changes in the adsorption energy and dissociation barrier of O_2, within the expected DFT error, lead to correct linear regime, which results in substantially better quantitative agreement with experiments. We rationalized these changes on the basis of microkinetic models previously proposed for this system and found that an accurate description of O_2 adsorption and dissociation is crucial to correctly model this catalytic system.

Acknowledgements S.P. acknowledges the CNR 2013 Short Term Mobility Program for partial financial support. The authors acknowledge the use of the UCL Legion High Performance Computing Facility (Legion@UCL), and associated support services, in the completion of the computational part of this work.

References

1. Engel T, Ertl G (1978). J Chem Phys 69:1267-1281
2. Klikovits J, Napetschnig E, Schmid M, Seriani N, Dubay O, Kresse G, Varga P (2007). Phys Rev B 76:045405
3. Hendriksen BLM, Bobaru SC, Frenken JWM (2004). Surf Sci 552:229-242
4. Chen MS, Cal Y, Yan Z, Gath KK, Axnanda S, Goodman DW (2007). Surf Sci 601:5326-5331
5. Gao F, McClure SM, Cai Y, Gath KK, Wang Y, Chen MS, Guo QL, Goodman DW (2009). Surf Sci 603:65-70
6. Hoffmann MJ, Scheffler M, Reuter K (2015). Acs Catal 5:1199-1209
7. Gabasch H, Knop-Gericke A, Schlogl R, Borasio M, Weilach C, Rupprechter G, Penner S, Jenewein B, Hayek K, Klotzer B (2007). Phys Chem Chem Phys 9:533-540
8. Duan ZY, Henkelman G (2014). Acs Catal 4:3435-3443
9. Rogal J, Reuter K, Scheffler M (2008). Phys Rev B 77:155410
10. van Rijn R, Balmes O, Resta A, Wermeille D, Westerstrom R, Gustafson J, Felici R, Lundgren E, Frenken JWM (2011). Phys Chem Chem Phys 13:13167-13171
11. Stamatakis M (2013) *Zacros*: Advanced Lattice-KMC Simulation Made Easy. http://www.zacros.org.
12. Stamatakis M, Vlachos DG (2011). J Chem Phys 134:214115-214111–214115-214113
13. Nielsen J, d'Avezac M, Hetherington J, Stamatakis M (2013). J Chem Phys 139:224706-224701–224706-224713
14. Piccinin S, Stamatakis M (2014). Acs Catal 4:2143-2152
15. Stamatakis M, Piccinin S (2016). Acs Catal 6:2105-2111
16. Reuter K, Scheffler M (2006). Phys Rev B 73:045433
17. Stamatakis M, Vlachos DG (2012). Acs Catal 2:2648-2663
18. Grabow LC, Gokhale AA, Evans ST, Dumesic JA, Mavrikakis M (2008). J Phys Chem C 112:4608-4617
19. Brønsted JN (1928). Chem Rev 5:231-338
20. Evans MG, Polanyi M (1938). T Faraday Soc 34:0011-0023
21. Wu C, Schmidt DJ, Wolverton C, Schneider WF (2012). J Catal 286:88-94

22. Perdew JP, Burke K, Ernzerhof M (1996). Phys Rev Lett 77:3865-3868
23. Vanderbilt D (1990). Phys Rev B 41:7892-7895
24. Giannozzi P, Baroni S, Bonini N, Calandra M, Car R, Cavazzoni C, Ceresoli D, Chiarotti GL, Cococcioni M, Dabo I, Dal Corso A, de Gironcoli S, Fabris S, Fratesi G, Gebauer R, Gerstmann U, Gougoussis C, Kokalj A, Lazzeri M, Martin-Samos L, Marzari N, Mauri F, Mazzarello R, Paolini S, Pasquarello A, Paulatto L, Sbraccia C, Scandolo S, Sclauzero G, Seitsonen AP, Smogunov A, Umari P, Wentzcovitch RM (2009). J Phys-Condens Mat 21:395502
25. Henkelman G, Uberuaga BP, Jónsson H (2000). J Chem Phys 113:9901-9904
26. Piccinin S, Stampfl C (2010). Phys Rev B 81:155427
27. Luntz AC, Williams MD, Bethune DS (1988). J Chem Phys 89:4381-4396
28. Yates JT, Thiel PA, Weinberg WH (1979). Surf Sci 82:45-68
29. Davis JE, Nolan PD, Karseboom SG, Mullins CB (1997). J Chem Phys 107:943-952
30. Imbihl R, Demuth JE (1986). Surf Sci 173:395-410
31. Sjovall P, Uvdal P (1998). Chem Phys Lett 282:355-360
32. Falsig H, Hvolbaek B, Kristensen IS, Jiang T, Bligaard T, Christensen CH, Norskov JK (2008). Angew Chem Int Edit 47:4835-4839
33. McEwen JS, Bray JM, Wu C, Schneider WF (2012). Phys Chem Chem Phys 14:16677-16685
34. Pogodin S, Lopez N (2014). Acs Catal 4:2328-2332
35. Getman RB, Schneider WF, Smeltz AD, Delgass WN, Ribeiro FH (2009). Phys Rev Lett 102:076101
36. Eichler A, Mittendorfer F, Hafner J (2000). Phys Rev B 62:4744-4755
37. Honkala K, Laasonen K (2001). J Chem Phys 115:2297-2302
38. Carbogno C, Gross A, Meyer J, Reuter K (2003) in: Muino RD, Busnengo HF (eds) Dynamics of Gas-Surface Interactions: Atomic-Level Understanding of Scattering Processes at Surfaces, vol 50. Springer Series in Surface Science, Berlin,
39. Gross A, Eichler A, Hafner J, Mehl MJ, Papaconstantopoulos DA (2003). Surf Sci 539:L542-L548
40. Schimka L, Harl J, Stroppa A, Gruneis A, Marsman M, Mittendorfer F, Kresse G (2010). Nat Mater 9:741-744
41. Stegelmann C, Andreasen A, Campbell CT (2009). J Am Chem Soc 131:8077-8082
42. Boudart M, Rumpf F (1987). React Kinet Catal L 35:95-105
43. Xu XP, Goodman DW (1993). J Phys Chem-Us 97:7711-7718